Transient Combustion Responses of Homogeneous Propellants to Acoustic Oscillations in Axisymmetric Rocket Motors

T. S. Roh*and F. E. C. Culick†
California Institute of Technology
Pasadena, CA 91125

Abstract

A numerical analysis of unsteady motions in solid rocket motors has been conducted. The formulation considers a 2-D axisymmetric combustion chamber and a choke nozzle, and treats the complete conservation equations accounting for turbulence closure and finite-rate chemical kinetics in the gas phase and subsurface reactions. A fully coupled implicit scheme based on a dual time-stepping integration algorithm has been adopted to solve the governing equations and associated boundary conditions. Results of the steady-state calculations indicate that the distributions of pressure in the motor and Mach number in the nozzle are one-dimensional along the axial direction. Vorticity contours show similar pattern to those of Mach number in the combustion chamber. The nozzle has an influence on the flow and temperature fields in the combustion chamber. A narrow pressure pulse is imposed at the head end to simulate unsteady acoustic oscillations in the combustion chamber. When the front of the pulse reaches near the nozzle throat, pressure near the nozzle throat increases and blocks the hot gas flow from passing through the nozzle throat. Self-generated oscillations have similar frequencies to those of standing waves of the combustion chamber. Large vorticity fluctuations are observed in near surface region. The luminous flame zone responds to low-frequency pressure wave rather than high-frequency one. Temperature fluctuations in the primary flame zone of the head end oscillates independently of the imposed pressure oscillations while temperature fluctuations in downstream region show pressure-dependent oscillations.

I. Introduction

Combustion instabilities in solid propellant rocket motors have been extensively studied over several decades. The major obstacle in approaching the instability problem arises from difficulties in treating the various complicated physico-chemical processes involved in unsteady combustion of solid propellants. Specifically, interactions between chamber gas dynamics and transient combustion responses of the propellants need to be resolved in order to understand the key mechanisms responsible for driving instabilities in rocket motors. This provides the motivation for studying chamber flow dynamics and interactions between chemical processes and acoustic oscillations in combustion chambers.

Several modes of interactions between acoustic oscillations and transient combustion have been observed, the most important of which are pressure and velocity coupled responses,[1] denoting the sensitivity of combustion processes to local pressure and velocity fluctuations, respectively. While pressure coupling has been extensively studied and the origins of the physical behavior are reasonably well understood, the general problem of velocity coupling remains largely unresolved. Velocity coupling implies that transient combustion response is strongly influenced by the velocity oscillations parallel to the burning surface, rather than pressure oscillations.[2] The coupling is essentially a local phenomenon, depending on local flow structures, chemical reactions, gas-phase transport, acoustic oscillations, propellant properties, etc. Recent studies of turbulent transition behavior of the acoustic boundary layer[3,4] and the turbulent reactive acoustic boundary layer[5,6] have been conducted, revealed that the turbulent acoustic boundary layer on a solid propellant surface could be one of the primary mechanisms in velocity-coupled erosive burning. The modification of transport properties caused by turbulent fluctuations in the region between the gas phase flame and the propellant surface[7,8] is regarded as the underlying physical process in this type of velocity coupling. Beside pressure and velocity couplings, vorticity is considered as an interaction between acoustic oscillations and transient combustion. Since combustion processes on and near the burning surface control the radial velocity, vorticity fluctuations near the propellant surface are coupled with acoustic pressure and combustion process. Vorticity fluctuations are closely related to the fluctuating radial (or vertical) velocity component upon which system stability is so strongly dependent.[14]

*Post-Doctoral Scholar, AIAA member
†Professor, Fellow AIAA

In a series of studies on the interactions between acoustic motions and propellant combustion,[9–13] an analysis capable of treating complicated physico-chemical processes involved in unsteady combustion of homogeneous propellants has been developed for two-dimensional Cartesian and axisymmetric combustion chambers. Turbulence closure has been achieved by means of a well-calibrated two-layer model taking into account the effect of propellant surface transport properties. It has been shown that turbulence penetrates into the primary flame zone and consequently increases the propellant burning rate, a phenomenon commonly referred to as erosive burning. The oscillatory flow characteristics are significantly altered by the turbulence due to enhanced momentum and energy transport in the gas phase. A physical insight into the gaseous dynamics and unsteady propellant response has been obtained from analysis of unsteady motions in the combustion chamber. There, however, is a lack of exact simulation of real motor environments because computational domains exclude the nozzle section and forced oscillations are imposed at the chamber end. Therefore, the purpose of the present work is to conduct a more complete analysis of unsteady behavior in the axisymmetric rocket motor with a nozzle. Emphasis is placed on identifying various distinct features of internal flow-fields of the rocket motor in both steady and unsteady state calculations.

In subsequent sections, a theoretical formulation for homogeneous propellant combustion in 2-D axisymmetric rocket motors is established, followed by brief discussion of the computational domain and the numerical method used in this work. The steady-state flow-field is first obtained to provide the initial conditions for analysis of unsteady motions. A narrow pressure pulse is imposed at the head end to obtain a natural frequency of the concerned motor and to simulate acoustic oscillations in the combustion chamber. Various aspects of interactions among traveling acoustic oscillations, unsteady reacting flows, and transient propellant combustion are investigated systematically.

II. Theoretical Formulation

Figure 1 shows the situation examined here, an axisymmetric rocket motor. A choked nozzle is attached to the aft end of the combustion chamber. The combustion chamber consists of the gas phase and the condensed phase loaded with a double-base homogeneous propellant grain. The analysis of the gas-phase processes is based on the complete conservation equations of mass, momentum, energy, and species concentration, and takes into account finite-rate chemical kinetics and variations of thermo-physical properties with temperature. Turbulent transport is considered to discuss the effect of turbulent flow disturbances on unsteady heat-release mechanisms. In vector notation, the set of conservation equations for a 2-D axisymmetric combustion chamber including a multi-component chemically reacting system of N species, can be written as

$$\frac{\partial \mathbf{Q}}{\partial t} + \frac{\partial}{\partial x}(\mathbf{E} - \mathbf{E_V}) + \frac{\partial}{\partial y}(\mathbf{F} - \mathbf{F_V}) = \mathbf{S} \tag{1}$$

where x and y represent the axial and radial coordinates, respectively. The conserved variable vector $\mathbf{Q}$ is defined as

$$\mathbf{Q} = y\,[\rho, \rho u, \rho v, \rho e, \rho k, \rho \epsilon, \rho Y_i]^T \tag{2}$$

where the subscript i stands for the ith species, ranging from 1 to $N-1$, and the superscript T denotes the transpose of the vector. In these equations, ρ, u, v, k, ϵ, and Y_i represent the density, axial and radial velocity components, turbulent kinetic energy, dissipation rate of turbulent kinetic energy, and mass fraction of species i, respectively. Convective flux vectors $\mathbf{E}$ and $\mathbf{F}$ in the axial and radial directions, respectively, take the from

$$\mathbf{E} = y\left[\rho u, \rho u^2 + p, \rho uv, (\rho e + p)u, \rho uk, \rho u\epsilon, \rho u Y_i\right]^T \tag{3}$$

$$\mathbf{F} = y\left[\rho v, \rho uv, \rho v^2 + p, (\rho e + p)v, \rho vk, \rho v\epsilon, \rho v Y_i\right]^T \tag{4}$$

Diffusion-flux vectors $\mathbf{E_V}$ and $\mathbf{F_V}$ are defined below.

$$\mathbf{E_V} = [0, \tau_{xx}, \tau_{xy}, u\tau_{xx} + v\tau_{xy} + q_{e_x}, \tau_{xk}, \tau_{x\epsilon}, q_{i_x}]^T \tag{5}$$

$$\mathbf{F_V} = [0, \tau_{xy}, \tau_{yy}, u\tau_{xy} + v\tau_{yy} + q_{e_y}, \tau_{yk}, \tau_{y\epsilon}, q_{i_y}]^T \tag{6}$$

The normal and shear stress are given by

$$\tau_{xx} = 2\mu_e \frac{\partial u}{\partial x} - \frac{2}{3}\mu_e\left(\frac{\partial u}{\partial x} + \frac{\partial v}{\partial y}\right) \tag{7}$$

$$\tau_{xy} = \left(\frac{\partial u}{\partial y} + \frac{\partial v}{\partial x}\right) \tag{8}$$

$$\tau_{yy} = 2\mu_e \frac{\partial v}{\partial y} - \frac{2}{3}\mu_e\left(\frac{\partial u}{\partial x} + \frac{\partial v}{\partial y}\right) \tag{9}$$

where μ_e is the effective viscosity, which is expressed by

$$\mu_e = \mu_l + \mu_t \tag{10}$$

Subscriptions l and t represent laminar and turbulent parts, respectively. The thermal diffusion terms q_{e_x} and q_{e_y} include contributions from heat conduction and mass diffusion processes. Fick's law is used to approximate the species diffusion terms q_{i_x} and q_{i_y}. Turbulent diffusion fluxes are given as

$$\tau_{xk} = \left(\mu_l + \frac{\mu_t}{\sigma_k}\right)\frac{\partial k}{\partial x} \tag{11}$$

$$\tau_{yk} = (\mu_l + \frac{\mu_t}{\sigma_k})\frac{\partial k}{\partial y} \tag{12}$$

$$\tau_{x\epsilon} = (\mu_l + \frac{\mu_t}{\sigma_\epsilon})\frac{\partial \epsilon}{\partial x} \tag{13}$$

$$\tau_{y\epsilon} = (\mu_l + \frac{\mu_t}{\sigma_\epsilon})\frac{\partial \epsilon}{\partial y} \tag{14}$$

The source vector **S** includes all source terms associated with the axisymmetric geometry and all remaining terms.

$$\mathbf{S} = \begin{bmatrix} 0 \\ p - \frac{4}{3}\mu_e\frac{v}{y} + \frac{2}{3}\mu_e\frac{\partial u}{\partial x} - \frac{2}{3}v\frac{\partial \mu_e}{\partial y} \\ -\frac{2}{3}\frac{\partial}{\partial x}(\mu_e uv) - \frac{2}{3}\frac{\partial}{\partial y}(\mu_e v^2) \\ y(\mu_t G - \rho\epsilon) \\ y(C_{\epsilon 1}\mu_t G - C_{\epsilon 2}\rho\epsilon)\frac{\epsilon}{k} \\ yS_1 \\ \vdots \\ yS_N \end{bmatrix} \tag{15}$$

where

$$G = 2\left[\left(\frac{\partial u}{\partial x}\right)^2 + \left(\frac{\partial v}{\partial y}\right)^2\right] + \left(\frac{\partial u}{\partial y} + \frac{\partial v}{\partial x}\right)^2 \tag{16}$$

The eddy viscosity can be obtained from the Prandtl-Kolmogorov relation.

$$\mu_t = C_\mu\left(\frac{\rho k^2}{\epsilon}\right) \tag{17}$$

The empirical constants in the above equations have standard values, with $\sigma_k = 1.0$, $\sigma_\epsilon = 1.3$, $C_{\epsilon 1} = 1.44$, $C_{\epsilon 2} = 1.92$, and $C_\mu = 0.09$.

Turbulence closure has been achieved based on the two-layer model of Rodi[15] because of its superior performance over conventional low-Reynolds-number k-ϵ schemes in terms of numerical accuracy and convergence. For unsteady calculations, the empirical constants in the turbulent equations have been corrected based on the study of Fan and Lakshminarayana.[16]

For a multi-component mixture, pressure and temperature can be calculated iteratively from the following thermodynamic relation and equation of state.

$$e = \sum_{i=1}^{N} Y_i h_i - \frac{p}{\rho} + \frac{1}{2}\left(u^2 + v^2\right) \tag{18}$$

$$p = \rho R_u T \sum_{i=1}^{N} \frac{Y_i}{W_i} \tag{19}$$

where h_i and W_i are the specific enthalpy and molecular weight of the ith species, respectively.

Within the pressure and temperature ranges of practical rocket-motor environments, thermal conductivity and viscosity of each species are basically functions of temperature alone. They can be well approximated by fourth-order polynomials in temperature, with the coefficients of these polynomials supplied by McBride et al.,[17] valid for temperatures ranging from 300 to 6000 K. Thermal conductivity and viscosity are calculated using Wilke's mixing rule.[18]

Chemical Kinetics Model

Owing to the difficulties in establishing a complete chemical kinetics scheme and limitations of computational resources, a thorough consideration of all physical and chemical processes does not appear feasible. A reduced reaction mechanism is therefore used to describe the combustion wave structure in both the gas and condensed phases. The chemical kinetics used here follow the model established in Ref. 12. This model is a viable alternative which provides well-resolved and reasonably accurate information about major chemical kinetic pathways.

Condensed-Phase Process

The condensed phase consists of a preheated zone and a superficial degradation layer in which both thermal decomposition of the propellant and reaction of the decomposed species takes place simultaneously. If we ignore the bulk motion, mass diffusion, and axial thermal diffusion, and assume constant thermo-physical properties, the condensed-phase processes are governed by a set of one-dimensional equations in the radial direction.

$$\dot{m} = \rho_c r_b \tag{20}$$

$$\rho_c C_c\frac{\partial T}{\partial t} + \dot{m}C_c\frac{\partial T}{\partial y} = \lambda_c\frac{1}{y}\frac{\partial}{\partial y}(y\frac{\partial T}{\partial y}) + \dot{q}_c \tag{21}$$

Here ρ_c denotes propellant density, r_b burning rate, and $\dot{m}$ mass flow rate on the burning surface. The rate of condensed-phase heat release per unit volume, $\dot{q}_c$, is determined by chemical reactions in a thin layer of propellant surface. The boundary condition associated with Eq. (21) at the condensed-phase far-field is $T = T_i$, where T_i is the initial (conditioned) temperature of the propellant. The surface conditions require that $T = T_s$, where T_i is the burning surface temperature.

Boundary Conditions

The processes in the gas and condensed phases are matched at the propellant surface by requiring continuity of mass and energy. This procedure ultimately

determines the propellant burning rate, temperature, and species concentrations at the surface. Conservation laws are applied to mass and species balances at the gas-solid interface. For unsteady calculations, the energy balance at the interface is expressed as

$$\lambda_c \frac{\partial T}{\partial y} = \lambda_g \frac{\partial T}{\partial y} + \dot{m}[\bar{Q}_s + (Cp_c - Cp_g)(T_s - \bar{T}_s)] \quad (22)$$

where $\bar{Q}_s$, $\dot{m}$, λ and C_p represent net surface heat release, mass flow rate, thermal conductivity and specific heat, respectively. The subscripts s, c and g denote burning surface, condensed phase and gas phase, respectively.

Additionally, the no-slip condition along the axial direction is enforced on the propellant surface and the nozzle wall, where pressure is obtained from the momentum balance. Flow symmetry is assumed to specify the variables along the center line. Boundary conditions at the head end require that the pressure gradient and axial velocity be zero. A second-order extrapolation are adopted at the nozzle exit to obtain boundary variables in supersonic condition.

III. Calculations

Fig. 2 shows the computational grid system for the rocket motor examined here. The combustion chamber, has a mean pressure of 60 atm, is closed upstream, and measures 5.08 cm in diameter and 0.6 m in length. The computational grid for the combustion chamber consists of 50 × 80 points in the axial and radial directions, respectively, while the condensed-phase grid is composed of 50 × 50 points in the same respective directions. The nozzle contour is delineated by a third-order polynomial in the axial coordinate, with the throat diameter being 2.3 cm. The nozzle has 20 × 80 mesh points of computational grid. The grids of the combustion chamber are clustered near the burning surface in the radial direction to resolve the steep gradients of temperature and species concentrations occuring in the condensed-phase near field. The grid system in the nozzle are inversely stretched in the same rate as the combustion to represent viscous sublayer in the turbulent regime along the nozzle wall and highly clustered at the nozzle throat in the axial direction to properly catch fast varying variables. The computational domain for the condensed phase extends 100 μm into the propellant. The smallest grid spacings in the direction normal to the surface in the combustion chamber are about 0.7 μm and 0.1 μm in the gas and condensed phases, respectively. The maximum grid aspect ratio in the combustion chamber is around 10,000. The nozzle's smallest grid spacing near the wall is about 0.4 μm. Major ingredients of the propellant are 52% NC and 43% NG, and the thermochemical parameters used in the present study are listed in Ref. 12.

IV. Numerical Method

A convenient and systematic procedure to convert two-dimensional Cartesian codes into 2-D axisymmetric codes has been proposed.[19] Even though careful calculations of the volume and surface areas of the control volume is considered, a singularity problem is inevitably encountered in certain cases of 2-D axisymmetric calculations. In order to avoid this problem, the governing equations have been modified and solved as two-dimensional Cartesian equations.

$$\frac{\partial \hat{\mathbf{Q}}}{\partial t} + \frac{\partial}{\partial x}\left(\hat{\mathbf{E}} - \hat{\mathbf{E}}_\mathbf{v}\right) + \frac{\partial}{\partial y}\left(\hat{\mathbf{F}} - \hat{\mathbf{F}}_\mathbf{v}\right) = \mathbf{S_n} \quad (23)$$

where the superscript $\hat{}$ denotes that there is no y term in each vector, and the new source vector can be expressed as

$$\mathbf{S_n} = \hat{\mathbf{S}} - (\hat{\mathbf{F}} - \hat{\mathbf{F}}_\mathbf{v}) \quad (24)$$

This set of governing equations is solved numerically by means of a finite-volume approach. An dual time-stepping integration method[10] proven to be quite efficient and robust for reacting flows at all speeds has been adopted to study the unsteady behavior in the combustion chamber of the solid rocket motor. A fully-coupled implicit formulation is used to enhance numerical stability and efficiency.

V. Results and Discussions

The steady-state flow-field must be obtained first to provide the initial conditions for analysis of unsteady motions. Figure 3 shows contours of dynamic pressure and its distribution along the axial direction. The distribution of pressure is almost one-dimensional along the axial direction. Pressure quickly drops in the nozzle while it slightly decreases in the combustion chamber. Contours of Mach number and its distributions along the axial direction are shown in Fig. 4. The Mach number contours reveal a slowly varying mass-driven flow in the combustion chamber. The Mach number along the centerline increases almost linearly from zero at the head end to 0.2 at the chamber end. In the nozzle, the Mach number quickly rises in one-dimensional manner. The contour lines of Mach number near the junction between the combustion chamber and nozzle have wrinkles on them due to radial velocity discontinuity. Figure 5 reveals the contour plot of vorticity in combustion chamber. Vorticity contours show similar pattern to those of Mach number. Axial velocity plays an major role in determination of Mach number and vorticity because radial velocity is quite small compared to axial velocity in the combustion chamber.

Figure 6 presents the contour plots of turbulent kinetic energy and temperature distributions. The flow-

field and temperature distribution exhibit a multidimensional structure due to the effects of the turbulent flow. The broadening of the luminous flame and the disappearance of the dark zone in the downstream region are clearly observed. This spatial evolution of the flame structure is closely related to the development of turbulence in the combustion chamber. The contours of turbulent kinetic energy in the entire domain indicate an abrupt increase in turbulent intensity around x/L = 1/4, where the Reynolds number based on the centerline velocity is about 6,000. At the end of combustion chamber, the peak turbulent kinetic energy turns away from the surface because the hot gas flow inclines along the impermeable nozzle wall. Temperature contours bear similar evidence of the effect of the nozzle wall on the flow in combustion chamber.

Figure 7 shows the radial profiles of the turbulent Reynolds number at various axial locations. Turbulence begins to penetrate into the primary flame zone at the point where the crossflow (axial) mass flux over the surface reaches about 750 kg/m^2s, in agreement with the experimentally determined value for the onset of erosive burning.[20,23] The cross-flow velocity is a quantity closely related to the threshold behavior of erosive burning in solid propellants. The burning rate increases almost linearly with crossflow mass flux due to enhanced heat transfer by turbulence in the primary flame zone.

The effect of turbulence on the temperature field is clearly seen in Fig. 8, which shows the radial profiles of temperature at various axial locations. The temperature field is characterized by three distinct regimes corresponding to the primary flame, dark, and luminous flame zones. The motor internal flow exerts almost no influence on the combustion wave structure in the upstream region. The most significant observation, however, is that the dark zone gradually disappears in the downstream region. The luminous flame zone expands and eventually merges with the primary flame zone because of the turbulence-enhanced heat transfer in the dark zone, where the elevated temperature facilitates reduction of NO into final products.[10]

Figure 9 shows temperature contour plot of the condensed phase with axial distributions of surface temperature and burning rate on the propellant surface. The surface temperature imperceptibly decreases from the head-end region to the location X/L = 0.75 as pressure in the combustion chamber slightly decreases along the axial direction. Surface temperature and burning rate are strong function of pressure. The turbulence in the downstream region penetrates into the primary flame zone, enhancing mixing processes and modifying the local heat transfer rate at the propellant surface. The consequent increase in burning rate results from the increased surface temperature due to enhanced heat transfer from the gas phase. This shows that the primary flame behavior is most strongly related to the combustion characteristics of the condensed phase, rather than the luminous flame zone.[11,12]

After obtaining a steady state solution, a narrow pressure pulse is imposed at the head end to obtain a natural frequency of the concerned motor and to simulate acoustic oscillations in the combustion chamber. Figures 10 and 11 show the propagation of the pulse in the rocket motor. The frequency and magnitude of propagating pulse are around 3500 Hz and 1 % of the chamber pressure, respectively. When the front of the pulse reaches near the nozzle throat at t = 0.6 ms, pressure near the nozzle throat increases and blocks the hot gas flow from passing through the nozzle throat. Eventually, the pulse moves out of the nozzle without generation of any reflecting wave at t = 0.8 ms. Low-frequency pressure wave, however, wave generated at the end of the combustion chamber begins to propagate upstream. The frequency of this pressure wave is around 1800 Hz, half of the imposed pulse and is close to the frequency of the second mode standing wave of the combustion chamber only. The pressure wave at t = 1.3 ms reveals a property of a rigid surface reflection of the head end.

Figure 12 shows time evolutions of pressure oscillation and axial velocity fluctuations at axial location X/L = 0.125. The behavior of axial velocity fluctuations before t = 0.2 ms seems to follow the isentropic relation with the traveling pressure wave but the maximum of u' is bigger than a theoretical value. After a few trailing waves of the pulse, pressure oscillates in low-frequency manner even though the magnitude of oscillations is comparatively small. The frequency of the oscillations is around 900 Hz, the same as that of the first mode standing wave of the combustion chamber only. The region close to the surface responds to the pressure wave in phase-advance manner even though axial velocity change is small. Time evolutions of vorticity fluctuations at the same location are shown in Fig. 13. Large vorticity fluctuations are observed in near surface region opposite to the axial velocity fluctuations because only velocity changes in near surface region play an important role in vorticity fluctuations. In reality, axial velocity change along the radial direction in the core region is almost zero even though it looks much larger than that in near surface region. Figure 14 presents time evolutions of temperature fluctuations at the same location. The fact that large increase of temperature in the luminous flame zone is observed after t = 0.4 ms reveals the flame front responds to low-frequency pressure wave rather than high-frequency one. Temperature fluctuations in near surface region (primary flame zone), however, seem to oscillate regardless of frequencies of imposed pressure wave. Time evolutions of heat-release fluctuations at the same location represented in Fig. 15 show similar pattern to those of temperature

fluctuations regardless of flame zones. The behavior of the heat-release fluctuation closely follows the gradient of the temperature fluctuation, easily explained by the energy balance over a gas-phase control volume. Figure 16 shows time evolutions of the Rayleigh parameter, $< p'q' >$, fluctuations at same location. The effect of heat release on motor stability characteristics can be investigated using Rayleigh's criterion,[21,22] which determines the conditions for driving or suppressing flow oscillations when thermal energy is added (or subtracted) periodically to (or from) the acoustic field. Figures 17 - 21 for the axial location X/L=0.375 show similar characteristics to those of the axial location X/L=0.125.

Figure 22 shows time evolutions of pressure oscillation and axial velocity fluctuations at axial location X/L = 0.625. The behavior of axial velocity fluctuations before t = 0.6 ms seems to follow the isentropic relation with the traveling pressure wave and the maximum of u' is the same as a theoretical value. After a few trailing waves of the pulse, pressure oscillates in low-frequency manner. But this pressure wave is traveling upstream opposite to the pulse. The frequency of the oscillations is around 1800 Hz, the same as that of the second mode standing wave of the combustion chamber only. Axial velocity fluctuations are 180 degree out of phase because pressure oscillations move to the head end opposite to the pulse. Same as the location X/L = 0.125, the region close to the surface responds to the pressure wave in phase-advance manner even though axial velocity change is small. Time evolutions of vorticity fluctuations at the same location are shown in Fig. 23. Large vorticity fluctuations are observed in near surface region, same as the location X/L = 0.125 Figure 24 presents time evolutions of temperature fluctuations at the location X/L = 0.625. The position of large temperature fluctuations reveals that the luminous flame zone merges with the primary flame zone. After t = 0.7 ms, temperature fluctuations are affected by the up-going pressure wave in exactly same trend as axial velocity fluctuations. Time evolutions of heat-release fluctuations at the same location represented in Fig. 25 show similar pattern to those of temperature fluctuations regardless of flame zones. Figures 27 - 31 for the axial location X/L=0.8 show similar characteristics to those of the axial location X/L=0.625.

Figure 32 shows time evolutions of surface temperature fluctuations at the various locations. Primary flame behavior is most strongly related to the combustion characteristics of the condensed phase. In Figs. 14 and 19, temperature fluctuations in the primary flame zone oscillates independently of the imposed pressure oscillations. Temperature fluctuations in Figs. 24 and 29, however, show pressure-dependent oscillations. Merged flame zone moved toward the propellant surface according to increase of turbulence intensity, eliminates the property of the primary flame zone. Therefore, surface temperature without turbulence effect is more sensitive to temperature fluctuations in the primary flame zone then that with turbulent effect.

VI. Conclusions

A numerical analysis of unsteady motions in solid rocket motor with a nozzle has been conducted. The formulation considers a 2-D axisymmetric combustion chamber and treats the complete conservation equations, accounting for turbulence closure and finite-rate chemical kinetics in the gas phase and subsurface reactions. The governing equations have been modified and solved as two-dimensional Cartesian equations. A fully-coupled implicit scheme based on a dual time-stepping integration algorithm has been adopted to solve the governing equations and associated boundary conditions.

Results of the steady state calculations show various aspects of internal flow-field of the rocket motor. The distributions of pressure in the motor and Mach number in the nozzle are one-dimensional along the axial direction. Vorticity contours show similar pattern to those of Mach number in the combustion chamber. The nozzle has an influence on the flow and temperature field in the combustion chamber. The onset of turbulent flow occurs in the middle of the combustion chamber and changes the flame structure in the downstream region. The dark zone gradually disappears in the downstream region due to the effect of turbulence on the temperature field. The penetration of turbulence into the primary flame zone is responsible for increases in surface temperature and burning rate in the downstream region of the combustion chamber.

After obtaining a steady state solution, a narrow pressure pulse is imposed at the head end to obtain a natural frequency of the concerned motor and to simulate acoustic oscillations in the combustion chamber. When the front of the pulse reaches near the nozzle throat, pressure near the nozzle throat increases and blocks the hot gas flow from passing through the nozzle throat. Eventually, the pulse moves out of the nozzle without generation of any reflecting wave. Self-generated oscillations have similar frequencies to those of standing waves of the combustion chamber. Large vorticity fluctuations are observed in near surface region. The luminous flame zone responds to low-frequency pressure wave rather than high-frequency one. Temperature fluctuations in the primary flame zone of the head end oscillates independently of the imposed pressure oscillations while temperature fluctuations in downstream region show pressure-dependent oscillations.

References

[1] Culick, F. E. C., "Stability of Longitudinal Oscillations with Pressure and Velocity Coupling in a Solid Propellant Rocket," *Combustion Science and Technology*, Vol.2, No. 4, 1970, pp. 179-201.

[2] Price, E. W., "Velocity Coupling in Oscillatory Combustion of Solid Propellants," *AIAA Journal*, Vol. 17, 1979, pp. 799-800.

[3] Ma, T., Van Moorhem, W. K., and Shorthill, R. W., "An Innovative Method of Investigating the role of Turbulence in the Velocity Coupling Phenomenon," *Journal of Vibration and Acoustics*, Vol. 112, Oct., 1990.

[4] Ma, T., Van Moorhem, W. K., and Shorthill, R. W., "Experimental Investigation of Velocity Coupling in Combustion Instability," *Journal of Propulsion*, Vol. 7, No. 5, 1990.

[5] Roberts, T. A. and Beddini, R. A., "Response of Solid Propellant Combustion to the Presence of a Turbulent Acoustic Boundary Layer," *AIAA* 88-2942, July, 1988.

[6] Roberts, T. A. and Beddini, R. A., "A Comparison of Acoustic and Steady-State Erosive Burning in Solid Rocket Motors," *AIAA* 89-2664, July, 1989.

[7] Bulgakov, V. K., Karpov, A. I., and Lipanov, A. M., "Numerical Studies of Solid Propellant Erosive Burning," *Journal of Propulsion and Power*, Vol. 9, No. 6, 1993.

[8] King, M. K., "Erosive Burning of Solid Propellants," *Journal of Propulsion and Power*, Vol. 9, No. 6, 1993.

[9] Culick, F. E. C. and Yang, V., "Prediction of the Stability of Unsteady Motions in Solid Propellant Rocket Motors," *Nonsteady Burning and Combustion Stability of Solid Propellants;* edited by L. De Luca, E. W. Price, and M. Summerfield, Progress in Astronautics and Aeronautics, Vol. 143, 1992, pp. 719-779.

[10] Tseng, I. S. and Yang, V., "Combustion of a Double-Base Homogeneous Propellant in a Rocket Motor," *Combustion and Flame*, Vol. 96, 1994, pp. 325-342.

[11] Roh, T. S. and Yang, V., "A Comprehensive Analysis of Combustion Instabilities of Homogeneous Propellants in A Rocket Motor," *AIAA Paper* 95-2863, 1995 (also submitted to *Journal of Propulsion and Power*).

[12] Roh, T. S., Tseng, I. S., and Yang, V., "Effects of Acoustic Oscillations on Flame Dynamics of Homogeneous Propellants in Rocket Motors," *Journal of Propulsion and Power*, Vol. 11, No. 4, July 1995.

[13] Roh, T. S. and Yang, V., "Numerical Analysis of Combustion Instabilities of Homogeneous Propellants in Axisymmetric Rocket Motors," *AIAA Paper* No. 96-2623, July 1996.

[14] Flandro, G. A., "Effect of Vorticity on Rocket Combustion Stability," *Journal of Propulsion and Power*, Vol. 11, No. 4, July 1995.

[15] Rodi, W., "Experience with Two-Layer Models Combining the $k - \epsilon$ Model with a One-Equation Model near the Wall," *AIAA Paper* No. 91-0216, 1991.

[16] Fan, S. and Lakshminarayana, B., "Low-Reynolds-Number $k - \epsilon$ Model for Unsteady Turbulent Boundary-Layer Flows." *AIAA Journal*, Vol. 31, No. 10, October 1993, pp. 1777-1784.

[17] McBride, B. J. and Gordon, S., *Computer Program for Calculation of Complex Chemical Equilibrium Compositions, Rocket Performance, Incident and Reflected Shocks, and Chapman-Jouguet Detonations*, NASA SP-273, March 1976.

[18] Reid, R. C., Prausnitz, J. M., and Poling, B. E., *The Properties of Gases and Liquids*, 4th Ed., McGraw-Hill Publishing Co., New York, NY, 1987, pp. 577-597.

[19] Yu, S., "Convenient Method to Convert Two-Dimensional CFD Codes into Axisymmetric Ones," *Journal of Propulsion and Power*, Vol. 9, No. 3, 1993, pp. 493-495.

[20] Yamada, K., Goto, M., and Ishikawa, N., "Simulative Study on the Erosive Burning of Solid Rocket Motors," *AIAA Journal*, Vol. 14, No. 9, 1976, pp. 1170-1176.

[21] Rayleigh, J. W. S., *Theory of Sound*, Vol. II., Dover, New York, 1954

[22] Culick, F. E. C., "A Note on Rayleigh's Criterion" *Combustion Science and Technology*, Vol. 56, 1987, pp. 159-166

[23] Osborn, J. R. and Burick, R. J., "Technique for the Measurement of the Erosive Burning Rate of Solid Rocket Propellants," *Second International Symposium on Nucleonics in Aerospace*, July 1967, pp. 87-94.

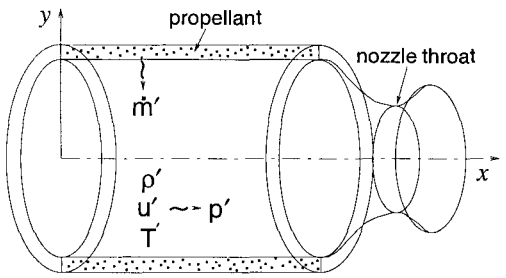

Figure 1: Schematic diagram of a solid rocket motor.

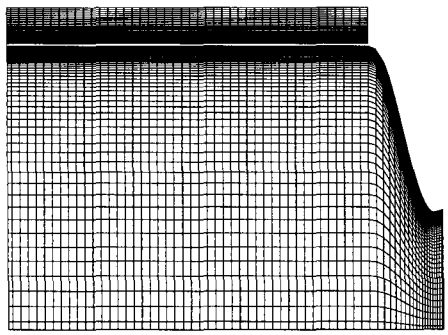

Figure 2: Grid distributions of computational domain

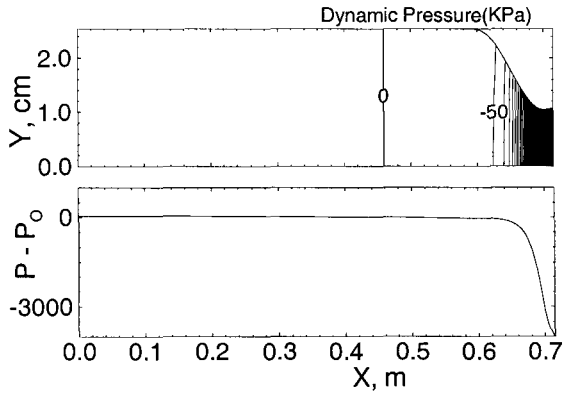

Figure 3: Contour plot of pressure and its distribution along axial direction

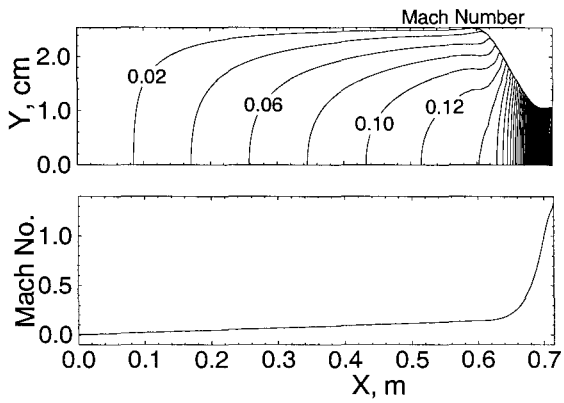

Figure 4: Contour plot of mach number and its distribution along axial direction

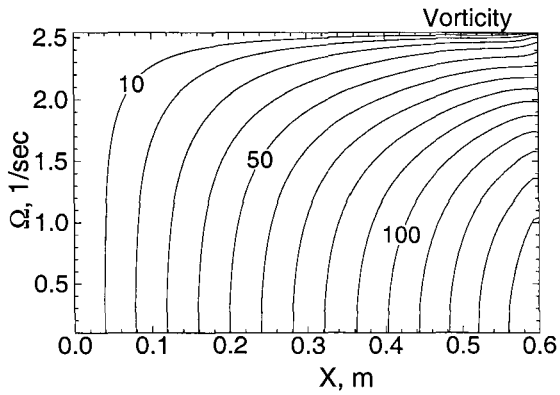

Figure 5: Contour plot of vorticity in combustion chamber

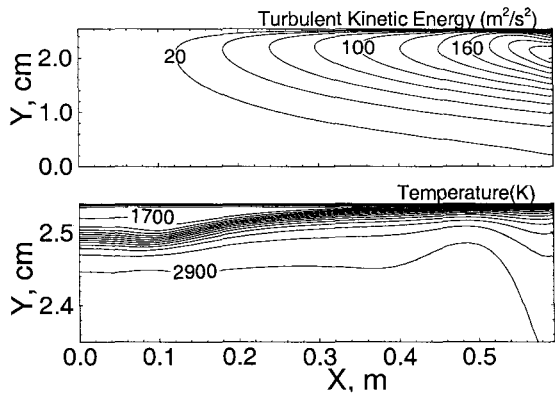

Figure 6: Contour plots of turbulent kinetic energy and temperature in combustion chamber

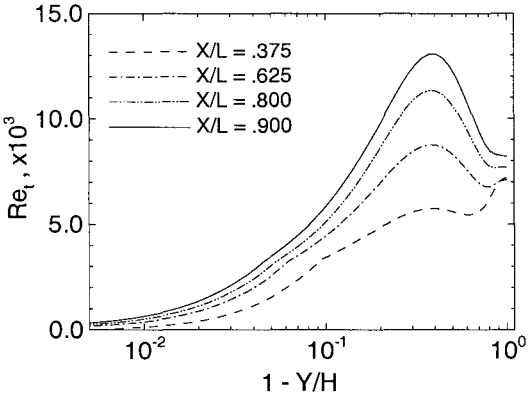

Figure 7: Radial distributions of turbulent reynolds number at various axial locations.

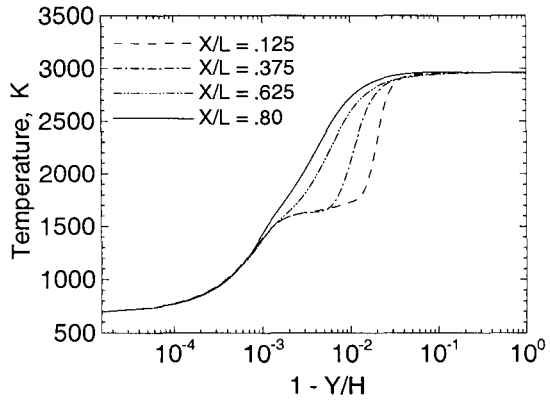

Figure 8: Radial distributions of temperature at various axial locations.

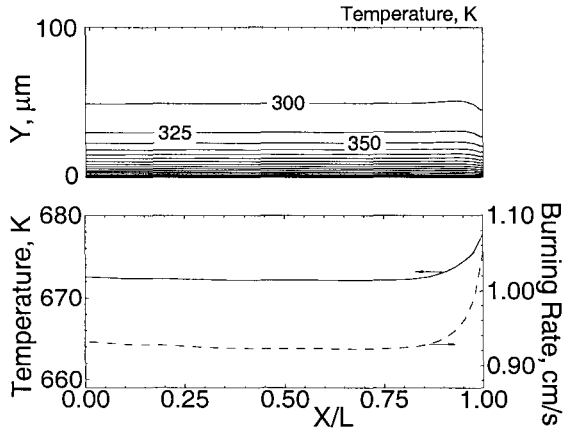

Figure 9: Contour plot of temperature in condensed phase and distributions of surface temperature and burning rate along axial direction.

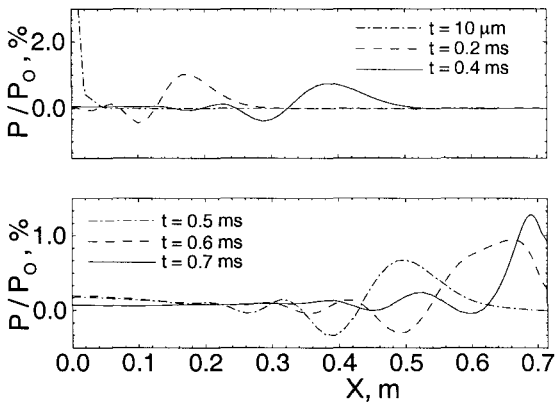

Figure 10: Propagations of pressure wave in rocket motor: t = 0 0.7 ms

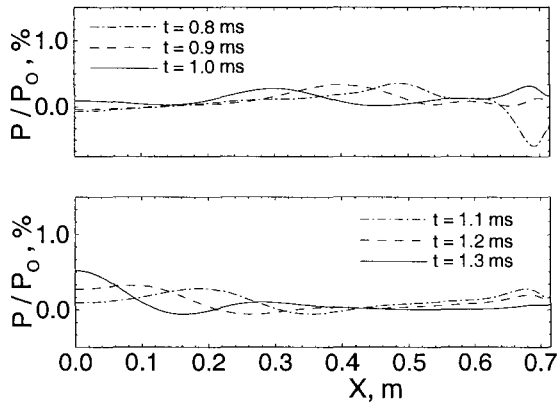

Figure 11: Propagations of pressure wave in rocket motor: t = 0.8 1.5 ms

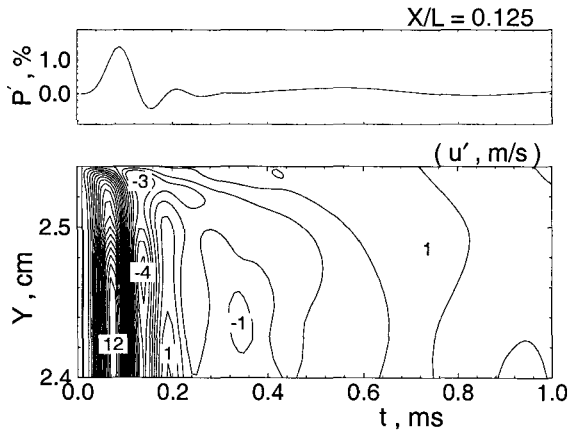

Figure 12: Time evolutions of pressure oscillation and axial velocity fluctuations at axial location X/L = 0.125

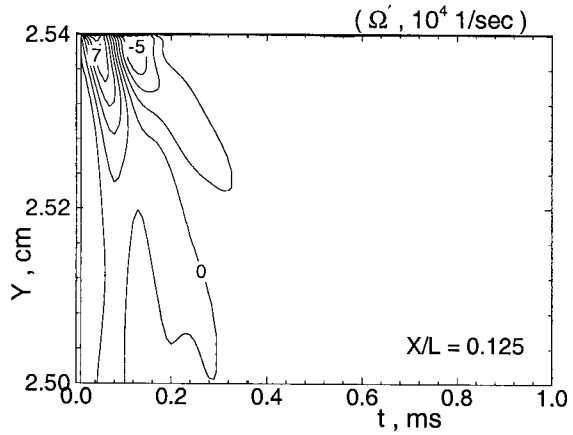

Figure 13: Time evolutions of vorticity fluctuations at axial location X/L = 0.125

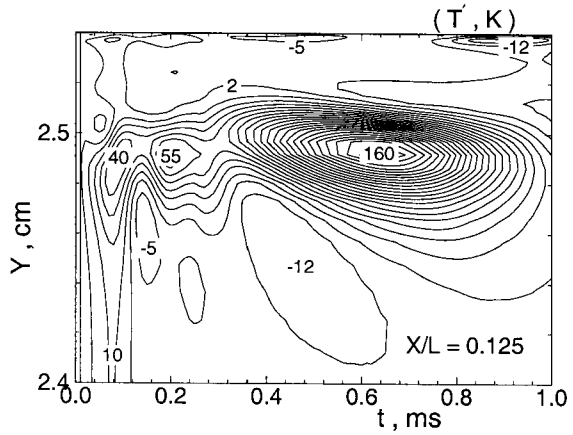

Figure 14: Time evolutions of temperature fluctuations at axial location X/L = 0.125

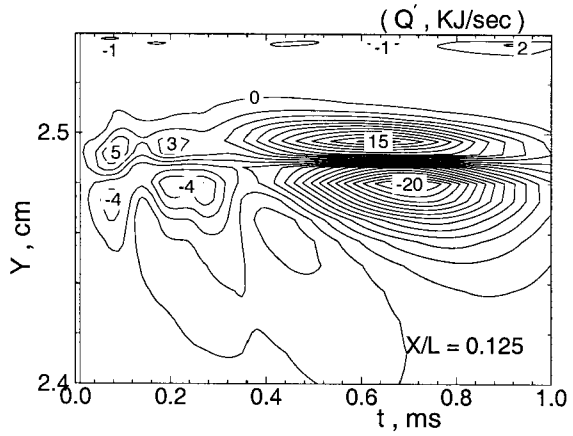

Figure 15: Time evolutions of heat-release fluctuations at axial location X/L = 0.125

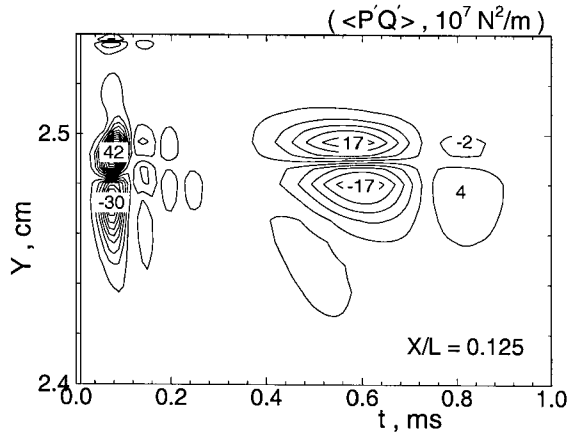

Figure 16: Time evolutions of $< p'q' >$ fluctuations at axial location X/L = 0.125

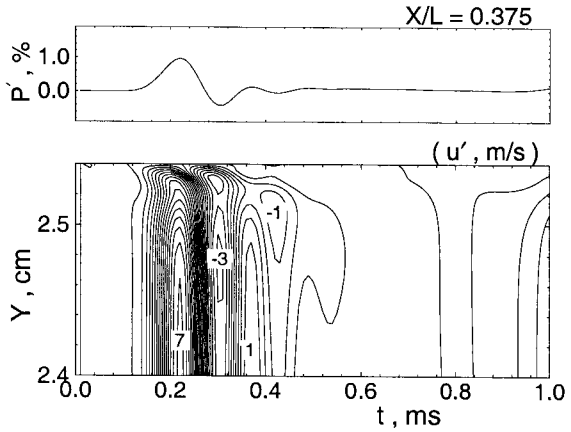

Figure 17: Time evolutions of pressure oscillation and axial velocity fluctuations at axial location X/L = 0.375

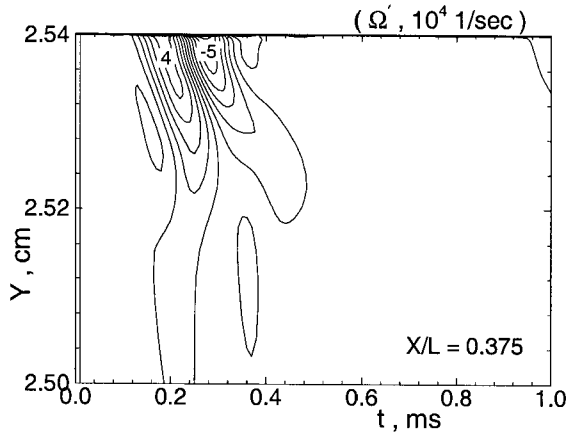

Figure 18: Time evolutions of vorticity fluctuations at axial location X/L = 0.375

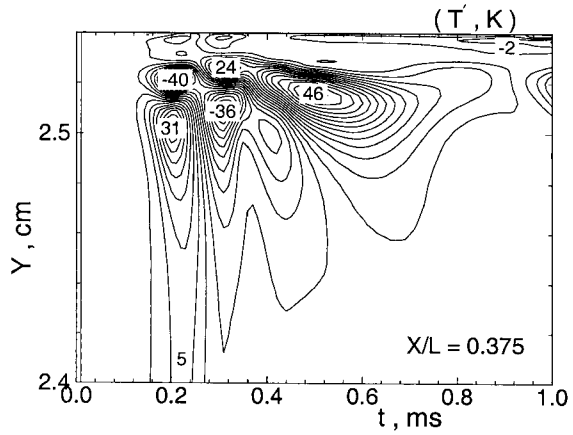

Figure 19: Time evolutions of temperature fluctuations at axial location X/L = 0.375

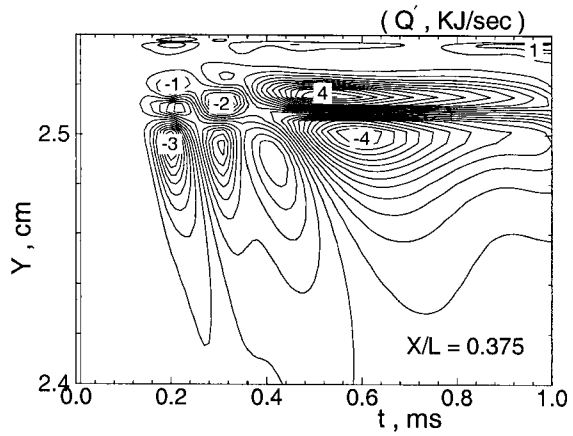

Figure 20: Time evolutions of heat-release fluctuations at axial location X/L = 0.375

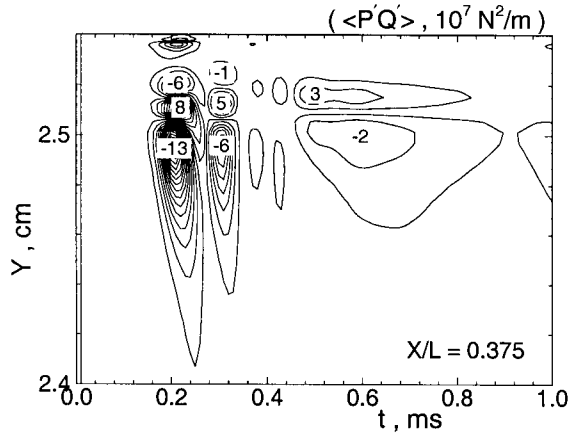

Figure 21: Time evolutions of $< p'q' >$ fluctuations at axial location X/L = 0.375

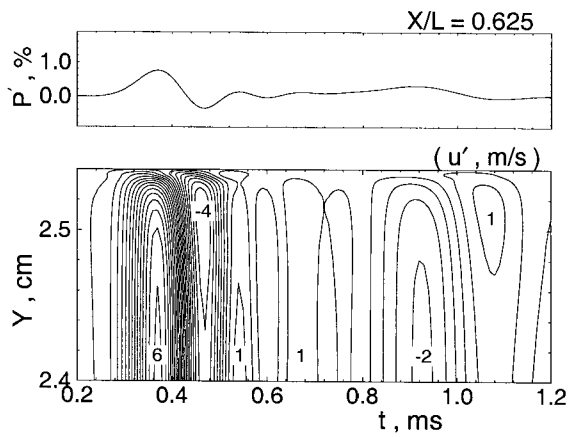

Figure 22: Time evolutions of pressure oscillation and axial velocity fluctuations at axial location X/L = 0.625

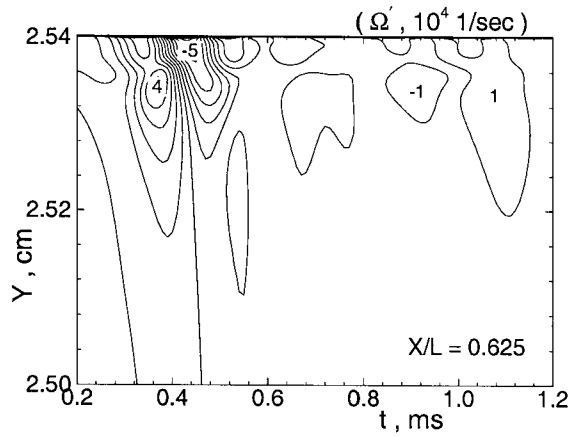

Figure 23: Time evolutions of vorticity fluctuations at axial location X/L = 0.625

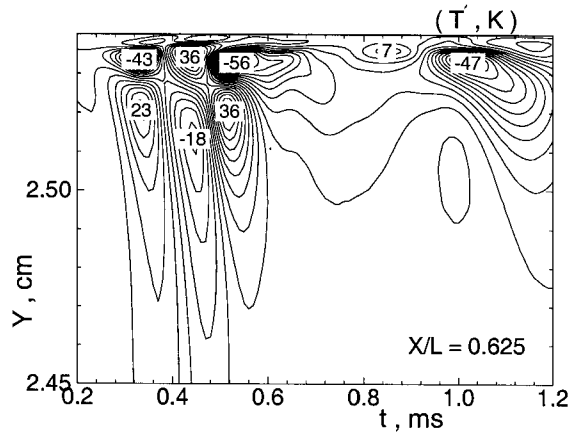

Figure 24: Time evolutions of temperature fluctuations at axial location X/L = 0.625

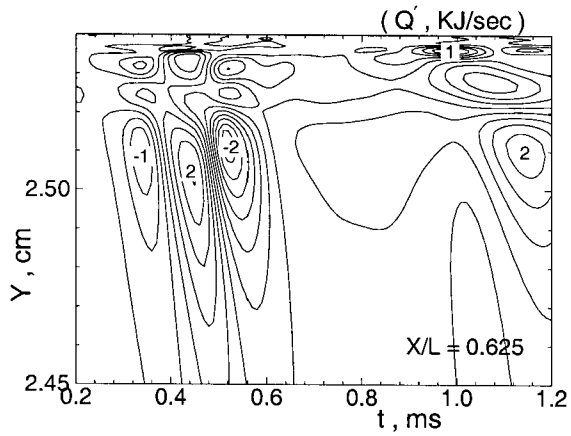

Figure 25: Time evolutions of heat-release fluctuations at axial location X/L = 0.625

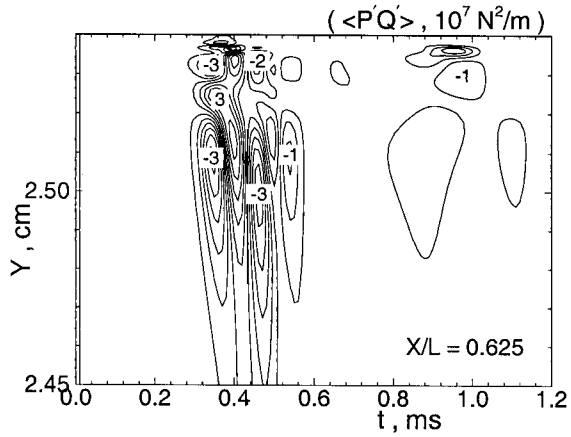

Figure 26: Time evolutions of $< p'q' >$ fluctuations at axial location X/L = 0.625

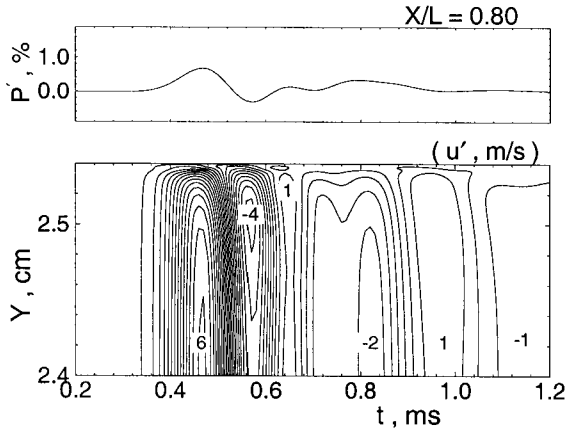

Figure 27: Time evolutions of pressure oscillation and axial velocity fluctuations at axial location X/L = 0.80

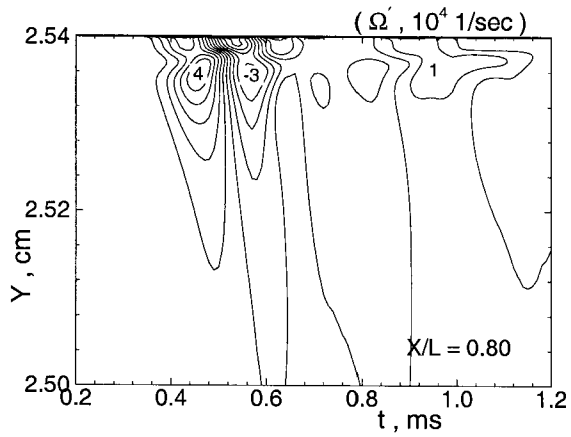

Figure 28: Time evolutions of vorticity fluctuations at axial location X/L = 0.80

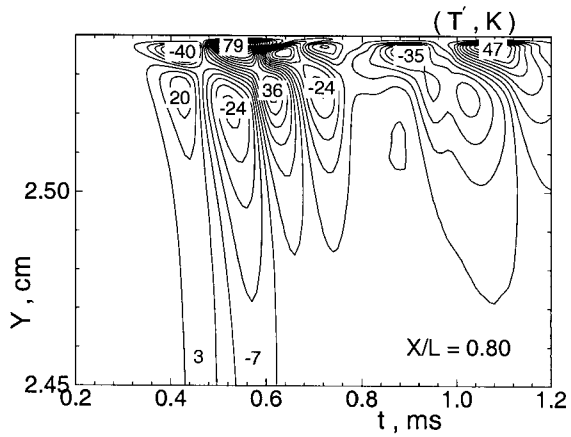

Figure 29: Time evolutions of temperature fluctuations at axial location X/L = 0.80

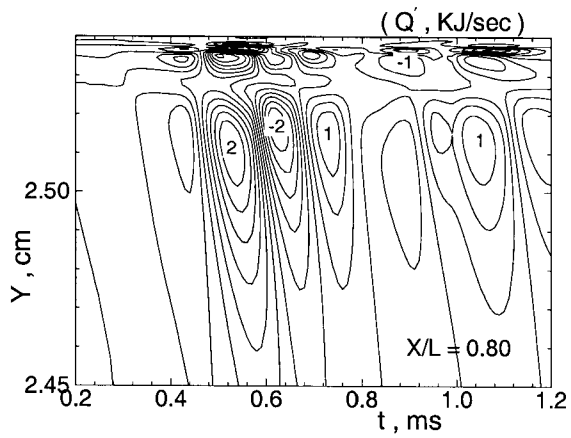

Figure 30: Time evolutions of heat-release fluctuations at axial location X/L = 0.80

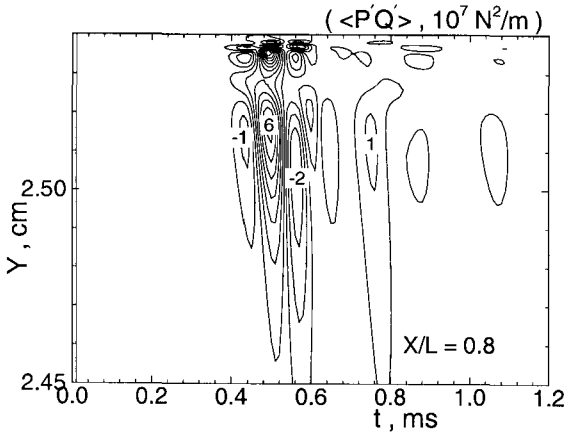

Figure 31: Time evolutions of $< p'q' >$ fluctuations at axial location X/L = 0.80

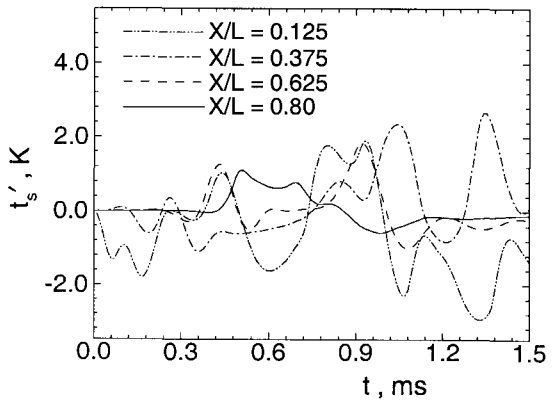

Figure 32: Time evolutions of surface temperature fluctuations at various axial location